Hindawi International Journal of Antennas and Propagation Volume 2023, Article ID 6682627, 14 pages https://doi.org/10.1155/2023/6682627



# Research Article

# **Experimental and Computational Analysis of Broadband THz Photoconductive Antennas**

Zachary Uttley, Jose Santos Batista, Bilal Pirzada, and Magda El-Shenawee

Department of Electrical Engineering, University of Arkansas, Fayetteville, AR, USA

Correspondence should be addressed to Zachary Uttley; zputtley@uark.edu and Magda El-Shenawee; magda@uark.edu

Received 22 December 2022; Revised 16 January 2023; Accepted 23 January 2023; Published 13 February 2023

Academic Editor: Claudio Gennarelli

Copyright © 2023 Zachary Uttley et al. This is an open access article distributed under the Creative Commons Attribution License, which permits unrestricted use, distribution, and reproduction in any medium, provided the original work is properly cited.

The work presents the fabrication and measurements of four LT-GaAs photoconductive terahertz (THz) antennas with different geometries of metallic electrodes. The goal is to analyze the overall bandwidth of the antennas through a comparison between the spectra of the generated photocurrent in the antenna gap, the radiated electric field THz pulse, and the S<sub>11</sub> parameter of the metallic electrodes. The photocurrent density and the S<sub>11</sub> parameters are computed using COMSOL multiphysics, while the generated THz pulse was experimentally measured using a time-domain spectroscopy system. The polarizations of the photoconductive antennas are experimentally measured, using x-cut quartz crystal halfwave plates, showing polarization in the direction of the electrode's long axis. Pinholes are used to verify system alignment and quality of the radiated signal spectra. The results show that the spectra of the radiated THz pulses in all four antennas considered in this work are dominated by the behavior of the S<sub>11</sub> parameter at the lower part of the frequency band, but with the decreasing photocurrent dominating the spectra at higher frequencies.

#### 1. Introduction

Recently, much progress has been achieved in the realm of THz signal generation using photoconductive antennas (PCAs) with a variety of applications in detection and imaging [1, 2]. Furthermore, the future development of 6G communication systems will need to reliably utilize frequencies and antennas in the THz range [3]. Due to the attractive characteristics and versatile usage of THz radiation, there has been an increase in research focused on realizing reliable photoconductive THz emitters with broader bandwidth and higher signal amplitude [1]. The mechanism for generating THz emission using PCAs works by exciting the photocarriers in a semiconducting substrate (e.g., LT-GaAs) using a pulsed femtosecond laser. The carriers are accelerated using a DC bias voltage applied to the metallic electrodes patterned on the surface of the substrate. The generated photocurrent pulse excites the antenna leading to radiation of the THz pulse. The generation of the photocarriers is achieved by using ultrashort mode-locked femtosecond laser pulses with measured width of ~92 fs

incident on the substrate [1, 4]. The concept of this mechanism is depicted in Figure 1.

An important characteristic of THz PCAs is the carrier lifetime of the active semiconducting substrate on which the electrodes are fabricated. The most used substrate is low-temperature grown Gallium Arsenide (LT-GaAs) due to its sub-picosecond carrier lifetime, high carrier mobility, and high resistivity reported in numerous papers (see, e.g., [1, 5]).

In this paper, we investigate the bandwidth and intensity of THz pulse generation using different geometries of metallic electrodes. We demonstrate that the PCA bandwidth is largely affected by the geometry of the metallic electrodes and the properties of the LT-GaAs substrate (i.e., mobility, carrier lifetime, and so on). The geometry of the metallic electrodes affects the resonant frequency of the antenna, while the substrate properties influence the generated photocurrent density pulse. Several unique electrode geometries have been reported, e.g., fractal and circular dipole, plasmonic-enhanced bowtie, Vivaldi, stripline, and spiral antennas [6–12]. Immense work has been accomplished

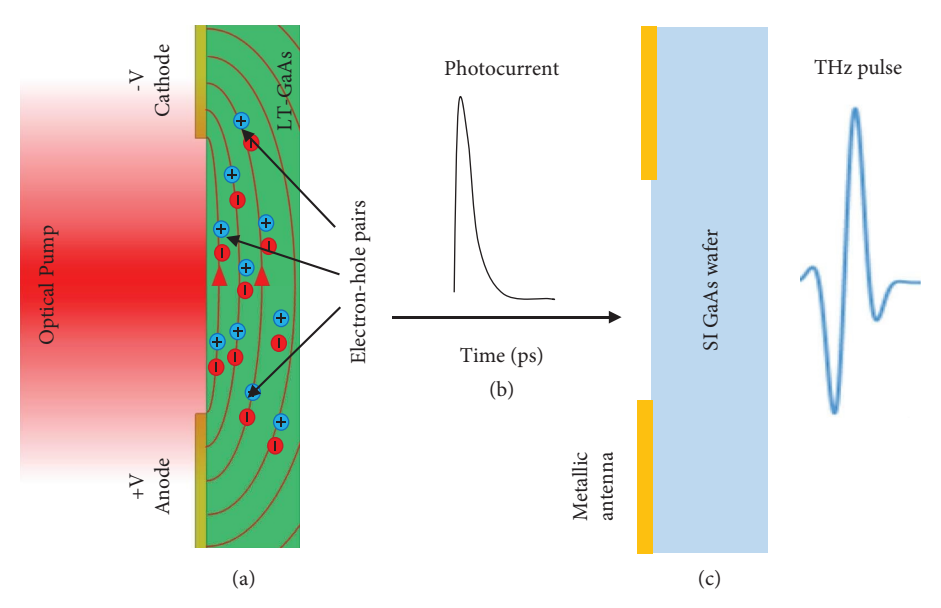


FIGURE 1: Conceptual diagram of THz generation in a PCA: (a) femtosecond laser beam excites electron-hole pairs in the LT-GaAs layer, (b) generated photocurrent pulse, and (c) metallic electrodes (antenna) excited by the photocurrent pulse in the gap to radiate THz pulse [1].

utilizing these geometries, among others, and has vastly improved the performance of THz emitters and detectors. Berry et al. increased the optical-to-THz efficiency of THz PCAs using plasmonic electrodes in conjunction with a logarithmic spiral antenna [8]. Furthermore, work from Burford et al. utilized plasmonic-thin-films and bowtie electrode geometry to produce PCAs with bandwidth up to ~5 THz [10]. In-depth modeling and simulation of THz PCAs using black phosphorus as the active semiconductor layer was conducted by Batista et al. showing improvement in bandwidth [11]. Hirota et al. generated and measured circular polarized THz radiation using a four-contact PCA and a total-reflection Si prism [12].

Here, various metallic electrode geometries of well-known broadband microwave antennas are investigated in experimental THz signal generation. The work involves fabrication and measurements of the PCAs. The goal is to analyze the factors that affect the bandwidth and intensity of the generated THz radiation. A time-domain spectroscopy (TDS) setup using a pulsed femtosecond laser with 780 nm wavelength and ~85 mW output power as an optical pump is utilized. An in-depth description of the specific TDS system used for measuring the performance of each fabricated PCA electrode design can be seen in [13].

Fabrication of THz PCAs can be accomplished through multiple means, the most common being photolithography, and electron beam lithography (EBL). Photolithography, using visible light and a photomask, is widely used in research and industry due to its rapid fabrication speed and relatively low cost [14]. Due to the nano-scale feature size in some THz PCA designs, notably plasmonic electrodes and nano-disc arrays, photolithography is not always preferred due to its resolution limitations but can be utilized for conventional PCAs [14]. EBL is a direct write technology that takes advantage of a magnetic field to steer a focused beam of electrons, patterning directly on the surface of a

resist-coated substrate [15]. Direct write capabilities of EBL, although more expensive and time-consuming than photolithography, allow for changes to be made to the PCA electrode design without the need to produce a new photomask, making rapid fabrication, and measurement possible.

The first goal here is to fabricate and experimentally measure the performance of four geometries of LT-GaAs PCAs. The bowtie, fractal, slotted, and circular metallic electrodes are selected for being known as broadband antennas in the microwave frequency band. The goal is to compare the THz signal generated from these antennas. The second goal is to investigate the factors that affect the overall bandwidth of the generated THz electric field pulse. Preliminary results were presented in [16].

#### 2. Methodology

The modeling using COMSOL multiphysics of the PCAs considered here is reported in [17]. The sketch in Figure 1 and the flowchart in Figure 2 demonstrate the three modules implemented to design the PCA emitter devices [10, 13]. The frequency-domain RF module solves the full wave equation to produce the maximum power absorbed in the LT-GaAs thin film layer. The semiconductor module solves the Poisson's/Drift equations for the carrier generation and the photocurrent volume density. The transient RF module solves the antenna radiation problem upon exciting the gap with the surface photocurrent density. The generated THz electric field pulse is given by [18, 19] as follows:

$$\mathbf{E}_{THz}(\mathbf{r},t) = -\frac{1}{4\pi\epsilon_0 c^2} \frac{\partial}{\partial t} \int \frac{\mathbf{J}_s(\mathbf{r}',t - (|\mathbf{r} - \mathbf{r}'|/c))}{|\mathbf{r} - \mathbf{r}'|} ds', \qquad (1)$$

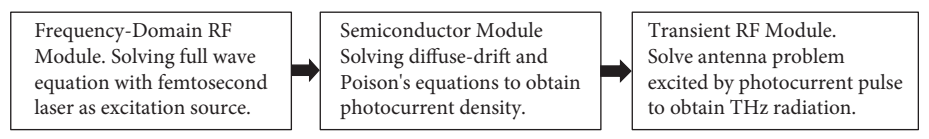


FIGURE 2: COMSOL multiphysics modules for PCAs [13].

where  $J_s$  is the surface current density, obtained upon adjusting the volume photocurrent density with the cross section of the antenna gap,  $\mathbf{r}$  is the position vector of the THz field,  $\mathbf{r}'$  is the position of the surface current density at each point in the surface of the gap ds, c is the speed of light in vacuum, and  $\epsilon_o$  is the permittivity of free space. The methodology section will be focused on the utilized techniques and challenges faced during the device fabrication of the PCAs considered here.

*2.1. Device Fabrication.* The process begins with an epitaxial (epi) layer growth of LT-GaAs onto a semi-insulating GaAs substrate. The growth specifications are as follows:  $350 \,\mu\text{m}$  semi-insulating GaAs (SI-GaAs) substrate,  $250 \,\text{nm}$  LT-GaAs epitaxy layer grown at  $250\,^{\circ}\text{C}$ , and annealed for 10 minutes at  $525\,^{\circ}\text{C}$ . These growth parameters are chosen to achieve a subpicosecond carrier lifetime and high mobility as reported in [20].

The wafer is sectioned into device-sized samples  $(5\,\mathrm{mm}\times 5\,\mathrm{mm})$ , each cleaned with a 4-minute bath in acetone, then isopropyl alcohol (IPA), both being carried out in an ultrasonic bath to aid in removing any debris from the sample. Each piece is then spin coated with a  $\sim 100\,\mathrm{nm}$  thick layer of poly (methyl methacrylate) A2 (PMMA A2) resist. After spin coating, the chip is placed on a hot plate for 4 minutes at  $180^\circ\mathrm{C}$  to harden the PMMA layer. Electron beam lithography (EBL) will be used to pattern the electrodes onto the resist layer. The electrode dimensions are defined in AutoCAD software, after which proximity effect correction (PEC) software is performed to improve the final device dimensional accuracy. Next, the pattern is written into the PMMA layer via EBL.

Once written, the pattern is developed via 60-second bath in methyl isobutyl ketone (MIBK), followed by a rinse in IPA after which the electrodes are metalized. Thermal evaporation is used to deposit a 5 nm adhesion layer of chromium (Cr) followed by a 50 nm layer of gold (Au). After metallization is completed, a standard acetone lift-off procedure is followed, which has been well documented in [21]. After being metalized, each device is mounted into a leadless chip carrier using clear nail polish as an adhesive. More details about the device dimensions and standard fabrication are shown in Appendix A.

To establish electrical connections for the applied bias voltage, wire bonding is performed using a wedge bonder with 1 mil aluminum bonding thread. To keep all measurements as consistent as possible, an identical fabrication procedure was followed for each electrode design, with all devices fabricated from the same wafer (wafer 2 in [16]). The carrier density of the LT-GaAs wafer was  $6.75 \times 10^{17} \, \text{l/m}^3$ , carrier lifetime was  $0.95 \, \text{ps}$ , and mobility was  $2392 \, \text{cm}^2/(\text{Vs})$ .

The four antennas fabricated and measured in this work are shown in Figure 3.

2.2. Fabrication Challenges. The first fabrication challenge was the overexposure of the PMMA resist during the EBL writing process. Overexposure from EBL is caused by electrons scattering off the substrate of the device, ultimately exposing areas of resist that should not have been. This effect is especially problematic when dealing with small features within largely exposed areas, such as the fractal cutouts, or the slot cutout, in most cases causing these features to be completely missing from the final pattern. To achieve the features from the CAD model, blank bowtie PCAs were fabricated, and then respun in a new PMMA layer and patterned with slots. This slot layer acted as an etch mask where Au and Cr etchants were used to remove the gold from the areas where the cutouts should be. Etching these features added complexity and steps to the fabrication process but achieved the desired results after finding the ideal etch time via try and error. Initially, using the manufacture's recommended etch times for a 50 nm gold layer, the device became completely overetched, as shown in Figure 4(a). Furthermore, time trials are shown in Figures 4(b)-4(e), with the arrow in Figure 4 indicates to etching defect. The results of Figure 4(e) reveal an ideal etch time of around 2.5 seconds, which we used in our device fabrication in this work.

The overexposure can also be compensated for by using proximity effect correction (PEC) software, where a CAD model can be fractured into cells, and the intensity of the electron beam can be modulated to reduce overexposure in problematic areas. The PEC software used in this work is Beamfox. An example of a fractured and modulated CAD file is seen in Figure 5, with the yellow color in Figure 5(b) indicates the lowest intensity and the blue color indicates to the highest intensity. Upon applying the PEC modulation, the overexposed areas marked in Figure 5(a) are all successfully patterned, with the increased sharpness in the small corners are marked in Figure 5(c). It was found that by using the PEC software, all features could be patterned without the need for etching. This solved the issue of overexposure and allowed for a simplified and streamlined fabrication process.

2.3. Experimental Setup and Measurements. To detect the radiated THz pulse of the fabricated PCAs, the TDS system described in [13] is utilized. Figure 6(a) shows the THz section of the system that includes a NIR lens, THz emitter, golden ellipsoidal mirrors, and THz detector. The yellow and blue dashed lines indicate the laser beam propagating out of the fiber optics cables to the emitter and detector, respectively. The femtosecond laser provides ~84 mW of power

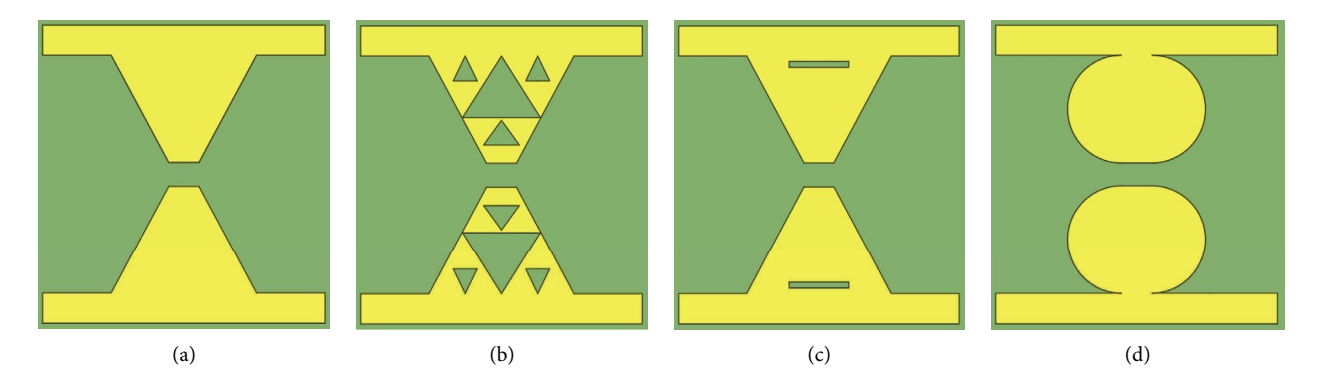


FIGURE 3: (a) Bowtie, (b) fractal, (c) slotted, and (d) circular PCAs.

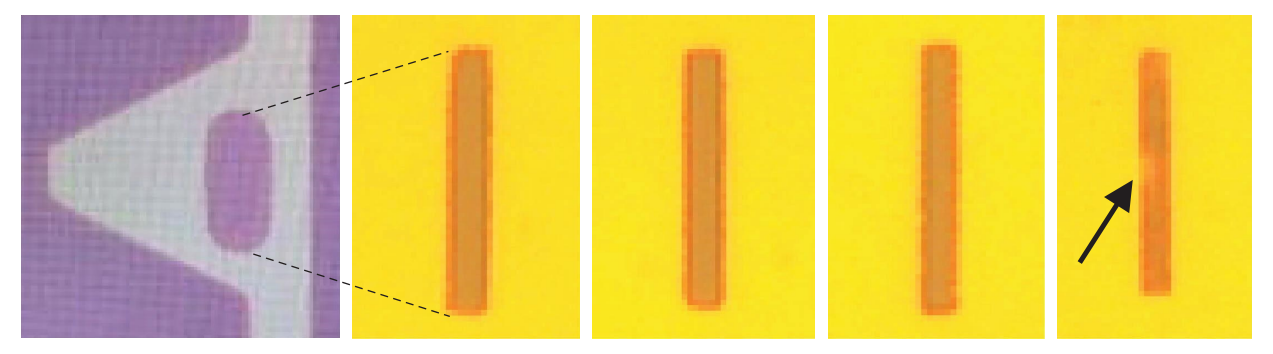


FIGURE 4: Slotted PCA (a) over etched slots. Slots etching time trials: (b) 5 seconds, (c) 3 seconds, (d) 2 seconds, and (e) 1 second. This etching test was conducted on silicon dioxide.

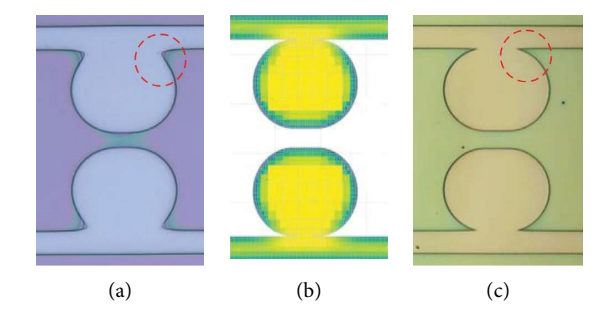


FIGURE 5: Circular PCA: (a) problematic uniform dosage, (b) PEC corrected CAD model, and (c) modulated dosage. These images were taken using an optical microscope. The difference in colors between 5(a) and 5(c) is due to the PMMA resist in 5(a) and the Cr/Au metallization in 5(c).

with a beam width of ~94 ps. The power of the laser beam incident to the  $5 \times 4 \, \mu \text{m}^2$  gap of in the PCA emitter is ~6 mW while it is 4.5 mW for the detector. An NIR lens of focal length 4.5 mm is used to focus the laser beam of ~3 mm spot size down to a ~5  $\mu$ m spot that is incident on the gap of the PCA. Two gold ellipsoidal mirrors, located in the center, guide the THz emission from the emitter to the detector. Between the two mirrors, a mount used for holding brass pinholes is shown in Figure 6(a).

The alignment of the laser to the PCA gap, as well as alignment of the THz beam, plays an integral role in the quality of the obtained THz signal. Figure 6(b) shows the alignment stages located at the emitter and detector sides. These stages allow for manipulation of the incident laser beam in 3 dimensions, the top three adjustment knobs being

for the laser alignment to the gap of the PCAs, while the bottom three knobs are to align the THz beam. Basically, each alignment stage has 3 degrees of freedom. The *z*-axis is used to focus the incoming laser to the correct size of the PCA gap, while the *x*- and *y*-axes are used to position the focused spot into the gap. A hyperhemispherical silicon lens is positioned in direct contact with the back of the PCA on both the emitter and detector to focus the THz beam. This lens is held in place by pressure between a metal flexure and the back of the PCA. It is imperative to ensure that the lens and PCA are in direct contact with no air gap between them.

Figure 6(c) demonstrates the reflection setup used for ensuring that the laser beam is incident on the gap of the PCA. The figure also shows the resulting reflected image of the gap on a paper card. While these reflected images are not

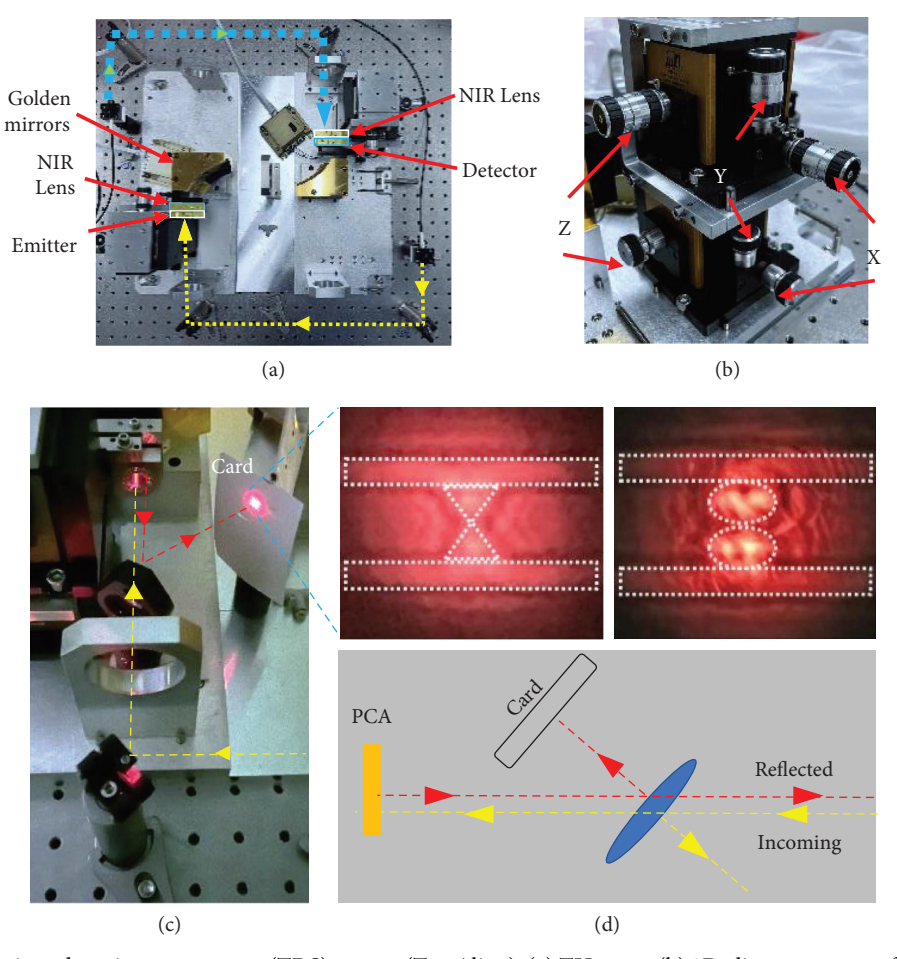


FIGURE 6: Photos of the time-domain spectroscopy (TDS) system (TeraAlign): (a) THz part, (b) 3D alignment stages for NIR (top) and THz (bottom), (c) reflection setup with bowtie (top) and circular (bottom) electrodes, and (d) diagram showing the function of a beam splitter used in (c).

high-resolution, one can make out the electrodes and transmission lines boundaries, which facilitates the initial alignment of the laser beam to the gap. From here, the laser spot can be further focused by sight. When focusing by sight is no longer feasible, the resulting pulse can be viewed in real time in the data acquisition software, while the alignment is further refined for an optimized THz signal. Reflection images of the bowtie and the circular emitters gaps are shown as examples. Figure 6(d) shows a representation of the beam paths through the beam splitter used in Figure 6(c). This diagram explains how the beam splitter interacts with the incoming and reflected laser beam to facilitate the projected image of the PCA onto a blank card.

The generated THz electric field pulse contains a broad range of frequencies, just viewing a pulse does not infer that the alignment is correct. For this reason, brass pinholes of diameters 0.5 and 1.0 mm are often utilized to verify that the THz beam is in its optimal position with respect to the detector [22]. Furthermore, using the pinholes remove low-frequency components of the signal [23]. Due to the large impact that the alignment quality has on the measurements, it is important to have reference devices with known pulse amplitude and spectrum to use as a calibration procedure before measuring the performance of the new

PCAs. After validating the alignment of the THz beam between the emitter and detector, the pinholes are removed, and the data are collected and shown in Section III. The fabricated 3D THz PCA emitter device stack is shown in Appendix A.

#### 3. Experimental Results and Discussion

3.1. PCAs Performance Measurements. The measurements results are obtained using the THz time-domain spectroscopy system reported in detail in [13]. Each electrode shape has been fabricated and mounted in the THz TDS system to measure the radiated THz electric field pulse and calculate its frequency-domain spectrum using the fast Fourier transform (FFT) using 2048 samples within a ~40 ps window. Performance can vary from device to device due to differences in the substrate properties, although sliced from the same wafer, as well as defects during fabrication. It should be noted that the devices were fabricated simultaneously in pairs. In Figure 7, the dimensions of the main trapezoid in the bowtie, fractal, and slotted electrodes are of the same size as shown in Figure 7(a). Here, we display only one of the electrodes due to the symmetry shown in Figure 3. The gap length

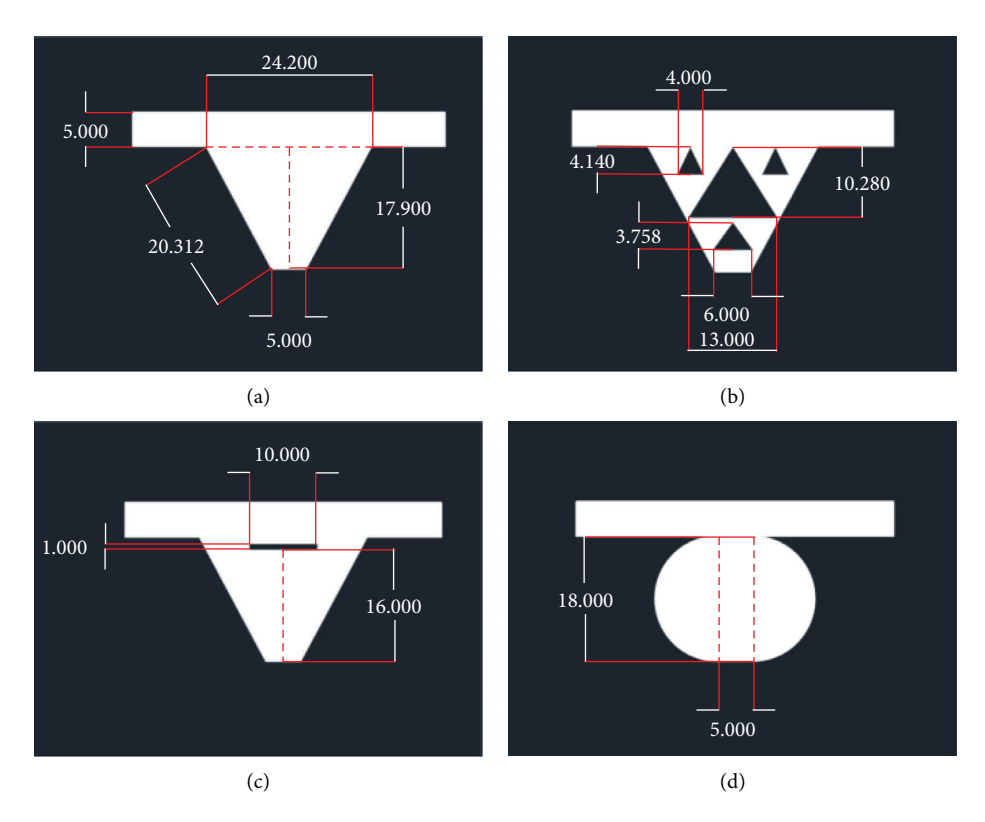


FIGURE 7: AutoCAD geometries and dimensions in µm of (a) bowtie, (b) fractal, (c) slotted, and (d) circular, metallic electrodes.

and width are kept at  $4 \mu m$  and  $5 \mu m$ , respectively, in all four PCAs shown in Figure 7.

The measured THz radiated electric field pulses in arbitrary units (a.u.) are shown in Figure 8 in the time and frequency domains. The x-axis in Figure 8 represents the time introduced by the optical delay lines in the TDS system to ensure that the femtosecond laser pulse reaches the emitter and detector at the same time. Shifting the delay lines within the system shifts the resulting pulse left or right on the plot. Figures 8(a) and 8(b) are the experimental measurements of the generated signals without going through any pinholes. Figures 8(c) and 8(d) are the experimental measurements when the generated THz signal travels through a pinhole of diameter 1 mm (cutoff frequency of ~0.175 THz). Figures 8(e) and 8(f) are the experimental measurements when the generated THz signal travels through a pinhole of 0.5 mm (cutoff frequency of ~0.351 THz). For comparison, a commercial PCA was measured and plotted in these figures. This commercial PCA was purchased from TeraView Ltd. and uses geometry protected under IP law. For clarification, the five THz measured pulses are deliberately shifted from each other in Figures 8(a), 8(c), and 8(d), respectively.

The results in Figure 8(a) show that the THz signal of the commercial PCA exhibits less peak-to-peak magnitude compared with the other four PCAs. However, the spectrum of the commercial PCA demonstrates a broader bandwidth compared with the other four PCAs as shown in Figure 8(b). To investigate the quality of the generated THz signals, we inserted a pinhole of diameter 1 mm in the center between the two golden ellipsoidal mirrors shown in Figure 6(a).

Note that the presence of the pinhole cuts the low-frequency components from all signals. In other words, the generated THz signals in the bowtie, slotted, fractal, and circular electrodes PCAs originally contained more low-frequency components compared with the commercial PCA, causing their peak-to-peak magnitudes to be larger than that of the commercial PCA as shown in Figure 8(a).

The results of using a 1 mm diameter pinhole are plotted in Figure 8(c) where the time-domain signal of the commercial PCA shows a larger peak-to-peak amplitude compared with the other four PCAs. The commercial PCA continued to demonstrate larger peak-peak-signal in the time domain upon passing the signals through a smaller pinhole of 0.5 mm diameter as shown in Figure 8(e). The spectra of all generated THz signals generated using all five PCAs and passing through the pinholes are shown in Figures 8(d) and 8(f), respectively. The spectrum plots of each device are extracted from the system, then normalized to their individual maximum value for convenient bandwidth comparison of their bandwidth.

It is noticed that the bandwidth of all spectra is similar for frequencies larger than 1 THz. However, for frequencies smaller than 1 THz, the generated THz signals in the bowtie, slotted, fractal, and circular seem to still contain more low-frequency components compared with the commercial PCA as shown in Figures 8(d) and 8(f). The results of Figure 8 demonstrate the necessity to analyze the bandwidth of all THz-generated signals as will be discussed in the following Section.

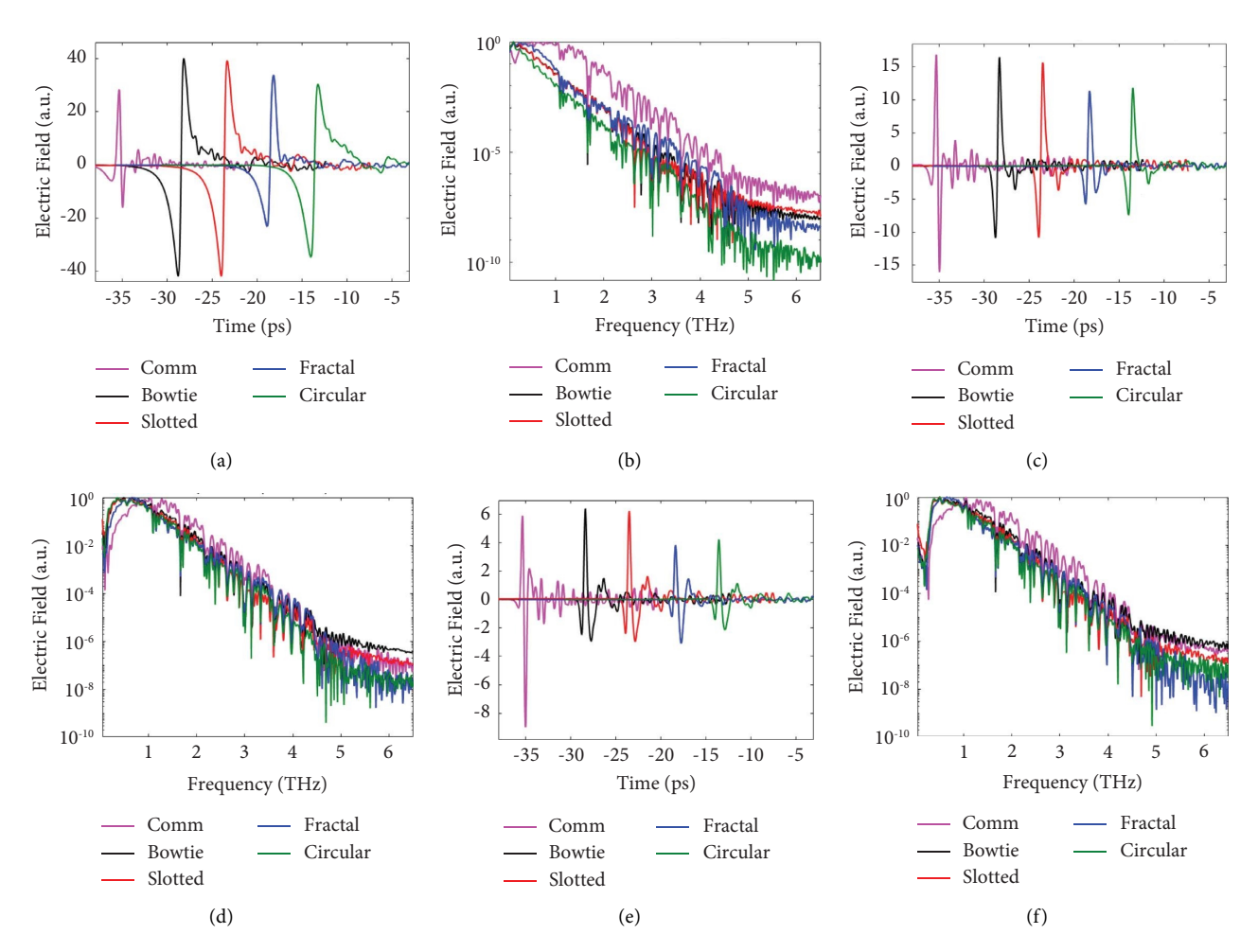


FIGURE 8: Experimental measurements of THz radiated signals of the bowtie, slotted, fractal, circular PCAs and a commercial PCA. (a) Time-domain pulses, (b) frequency-domain spectrum obtained using FFT. Both a and b are obtained without using pinholes. (c, d) Figures obtained using a 1 mm pinhole. (e, f) Figures obtained using a 0.5 mm pinhole. The spikes in the spectrum indicate to water signatures as experiments were conducted in the air without purging with nitrogen gas. Each spectrum is normalized to its maximum value.

3.2. Polarization Measurements and Far-Field Computation. To understand the amplitude variation of the generated THz time-domain signals shown in Figure 8(a), we employed two strategies. The first was based on experimental measurements of each antenna polarization, and the second was based on numerical simulation of the far electric field generated by each antenna using COMSOL Multiphysics.

3.2.1. Polarization Experimental Measurements. The polarization measurement results are shown in Figure 9 where the configuration used in the experiment is shown in Figure 9(a). The experiment utilized two wire grid polarizers and one x-cut quartz crystal halfwave plate. The later rotates the beam polarization by 90° at ~3.06 THz [24]. In this experiment, the THz beam propagates from the emitter to the detector through the first wire polarizer, the half-wave plate crystal, and finally the second wire grid as depicted in Figure 9(a). The detector is a commercial one with a horizontal polarization, purchased from TeraView Ltd. In the first experiment, the THz beam propagates through the wire

grid polarizer, oriented in the vertical direction, to allow the horizontal polarization signal to pass. The crystal is oriented such that no rotation occurs. Then, the second wire polarizer, oriented also in the vertical direction to pass the horizontal polarization to the detector. The resulting signals of the isolated horizontal polarization (H) are shown in Figures 9(b)-9(f) in red color plots. In the second experiment, the first polarizer is rotated 90° to pass the vertically polarized signal. The half-wave plate crystal is rotated 45° to convert the vertically polarized signal back to horizontal polarization to be measured by the detector. The second wire polarizer remains in the vertical direction as in the first experiment because the detector can only measure horizontally polarized signals. The results of the vertical polarization signals are shown in blue color plots in Figures 9(b)-9(f). The shaded light blue indicates the designed frequency of the half-wave plate of 3.06 THz. The comparison results between the measured polarization indicate that these antennas are mainly horizontally polarized since the horizontal plots are almost two orders of magnitude larger than the vertically polarized signals.

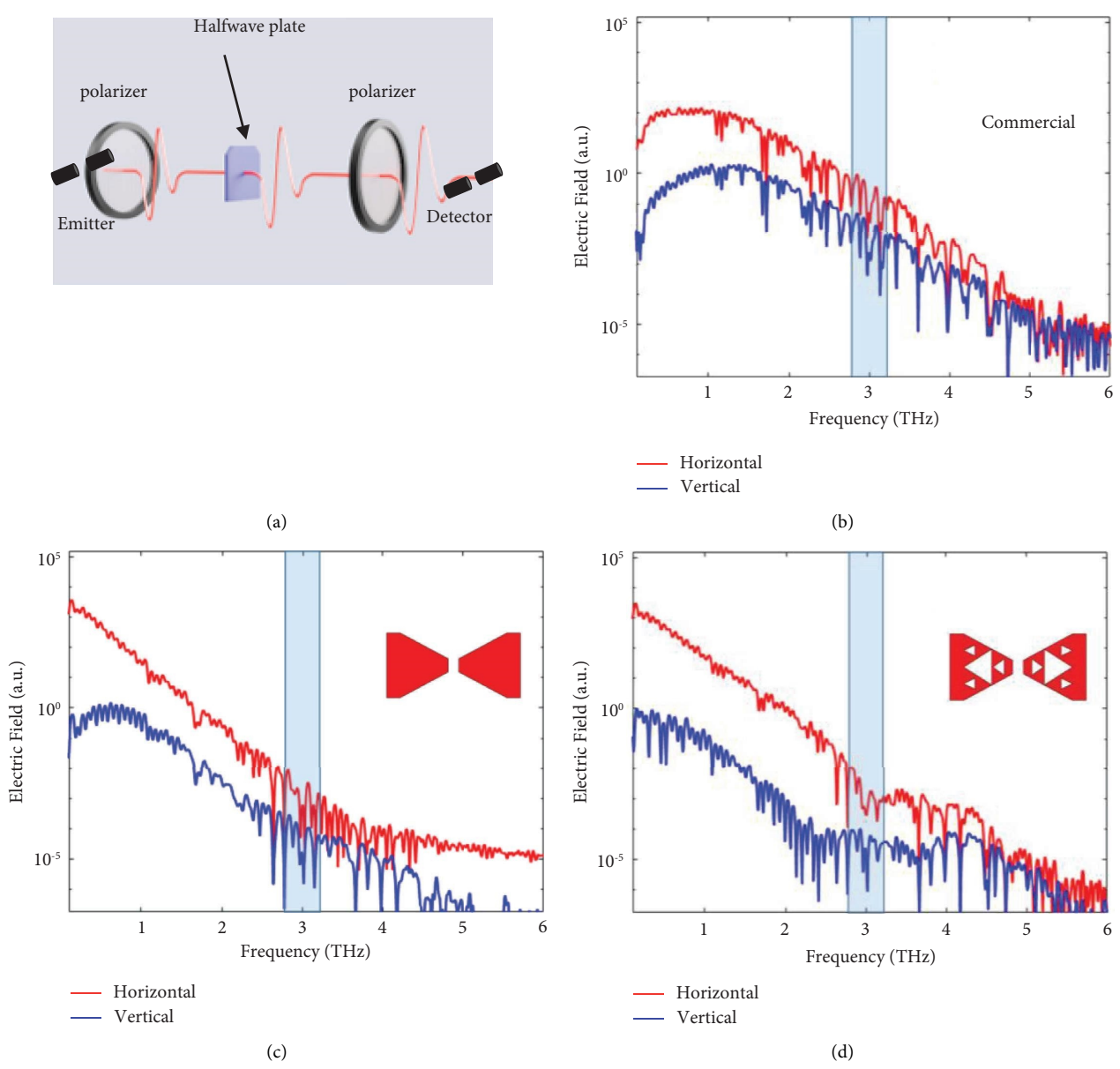


FIGURE 9: Continued.

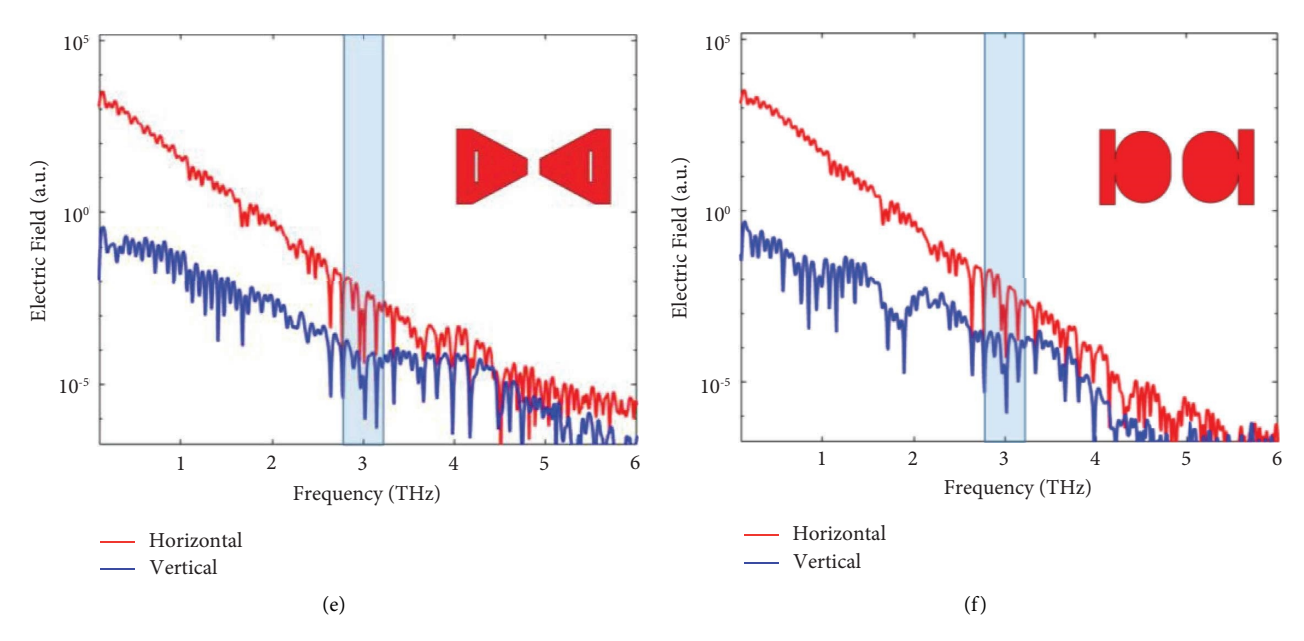


FIGURE 9: Experimental measurements of antenna polarization using two wire polarizers and a half-wave plate x-cut quartz crystal: (a) 3D experiment configuration, (b) commercial THz antenna from TeraView Ltd., (c) bowtie, (d) fractal, (e) sotted, and (f) circular, antennas. The dimensions of Figure 9(a) are not to scale, as the antennas are in micrometers, while the polarizers and the crystal are in centimeters.

3.2.2. Polarization COMSOL Computation. For consistency with the definitions of the horizontal and vertical polarizations used in Figure 9(a), here, we define the theta-polarization as horizontal polarization (H) and the phipolarization as vertical polarization (V) as shown in Figure 10. The far-field transformation in COMSOL was used to obtain the theta- and phi-polarizations at  $\theta = 90^{\circ}$  and  $\varphi = 0$ , and the results at 2 THz are summarized in Table 1. The distinguishing distance between the near and far-field regions was selected to be half wavelength (i.e.,  $75 \mu m$ ). The results show that the polarizations of these antennas are mainly in the horizontal direction as depicted in Figure 10. These computations are in full agreement with the experimentally measured results in Figure 9. It is important to clarify that the experimental system is not purged with nitrogen gas. As a result, the time-domain signal amplitude varies when conducting the measurements on different days due to the variation of humidity in the surrounding air. For example, while the results of Figure 9(a) show that a THz signal amplitude generated from the circular electrodes antenna is a bit smaller than that of the bowtie antenna, the opposite was observed in other repeated measurements (not shown here for space limitation). We fabricated and measured the THz signal of ~25 antennas of the various electrodes, and we observed a variation in the time-domain signal amplitudes. In addition, the alignment between the THz emitter and detector plays a significant role in the measured signal amplitudes.

3.3. Analysis of Overall Bandwidth. To understand the factors that influence the overall bandwidth of the PCA devices, the measured spectra of the generated THz signals, the COMSOL calculated S<sub>11</sub> parameters of each metallic

electrodes positioned on a semi-insulating GaAs substrate (as shown in Figure 1(c)), and the COMSOL calculated photocurrent density shown in Figure 11 are obtained. The volume photocurrent density, obtained upon solving the drift-diffuse equations using COMSOL [13], was multiplied by the cross-sectional area of the LT-GaAs layer  $(250 \text{ nm} \times 5 \mu\text{m})$  and then divided by the width of the electrodes (5 µm) to obtain surface current density in the gap shown in Figure 11. A 1V was used to bias the metallic electrodes for generating the photocurrent in the semiconductor module and then the current density pulse shown in the figure was used to feed the antenna gap in the RF Transient model as described in Figure 2. The results demonstrate that the generated photocurrent densities are approximately the same in all four devices, as expected since they have the same dimensions of the antenna gap and the thickness of the LT-GaAs layer. A variety of aspects of simulations and boundary conditions used in the COMSOL model can be seen in Appendix A and in [10, 11, 13, 17, 25].

The spectra comparison results are shown in Figure 12, where the dashed black line is  $-10\,\mathrm{dB}$ , a conventionally used value for determining antennas bandwidth. The shown  $S_{11}$  parameters of the bowtie, slotted, and fractal antennas demonstrate multiband nature. However, the  $S_{11}$  parameter of the circular antenna demonstrates a broader bandwidth starting at  $\sim 1.22\,\mathrm{THz}$  with a dip of  $\sim -40\,\mathrm{dB}$  at  $\sim 2.42\,\mathrm{THz}$ . The photocurrent spectra in Figure 12 show decreasing values with increasing frequency for all four devices. The spectra of the radiated THz signals in all four antennas seem to be dominated by the behavior of the  $S_{11}$  parameters at the lower part of the frequency band but with the decreasing spectra of the photocurrent density at higher frequencies. Upon comparing the overall bandwidths of the four PCAs using the  $-10\,\mathrm{dB}$  line, it is noticed that the bowtie provides

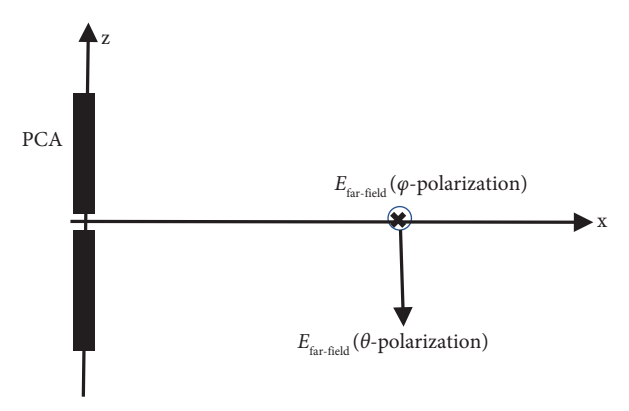


FIGURE 10: COMSOL calculation in the far-field at  $\theta = 90^{\circ}$  showing the theta- and phi-polarizations (equivalent to horizontal H and vertical V polarizations in the experiment).

Table 1: COMSOL far-field results at  $\theta = \pi/2$  and  $\varphi = 0$  and f = 2 THz.

	Bowtie	Slotted	Fractal	Circular
$E_{far-\theta}(V/m)$	0.7848	0.7377	0.7656	0.592
$E_{far-\Phi}(V/m)$	2.17e - 4	1.99e - 4	2.45e - 4	0.93e - 4

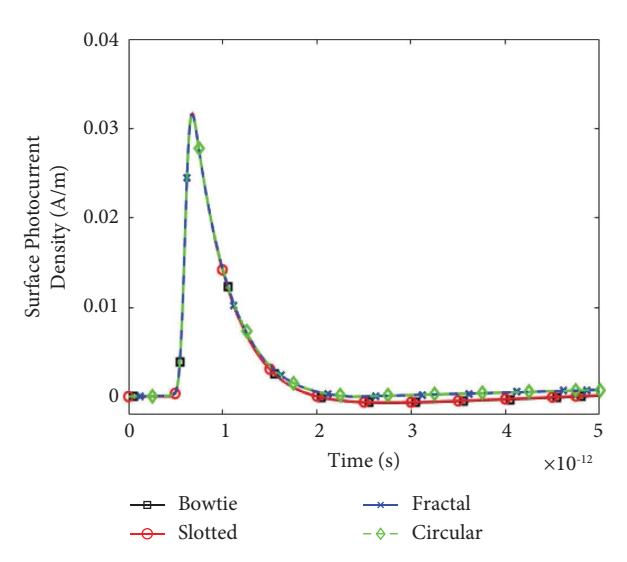


FIGURE 11: 3D modeled photoconductive surface current density of the four PCAs considered here. The electrodes were positioned on a multilayer of 250 nm LT-GaAs and half-space SI-GaAs, achieved in COMSOL by using a 400 nm thick layer and the scattering boundary condition.

two bands, one from 0.985 to 1.427 THz and the second band starts at 2.664 THz to beyond 6.5 THz. The fractal antenna also has two frequency bands, one from 0.998 to 1.239 THz and the second one starting at 2.921 to beyond 6.5 THz. The slotted antenna has two bands as well, one band from 0.998 to 1.51 THz and the second starts at 2.737 to

beyond the 6.5 THz. However, the circular antenna shows one broadband that starts at 1.22 THz to beyond the 6.5 THz. Considering the noise level of the measured THz signal in Figure 12, we observed that it is  $\sim$ -80 dB in the bowtie,  $\sim$ -90 dB in slotted and  $\sim$ -100 dB in the fractal PCAs and the circular PCAs.

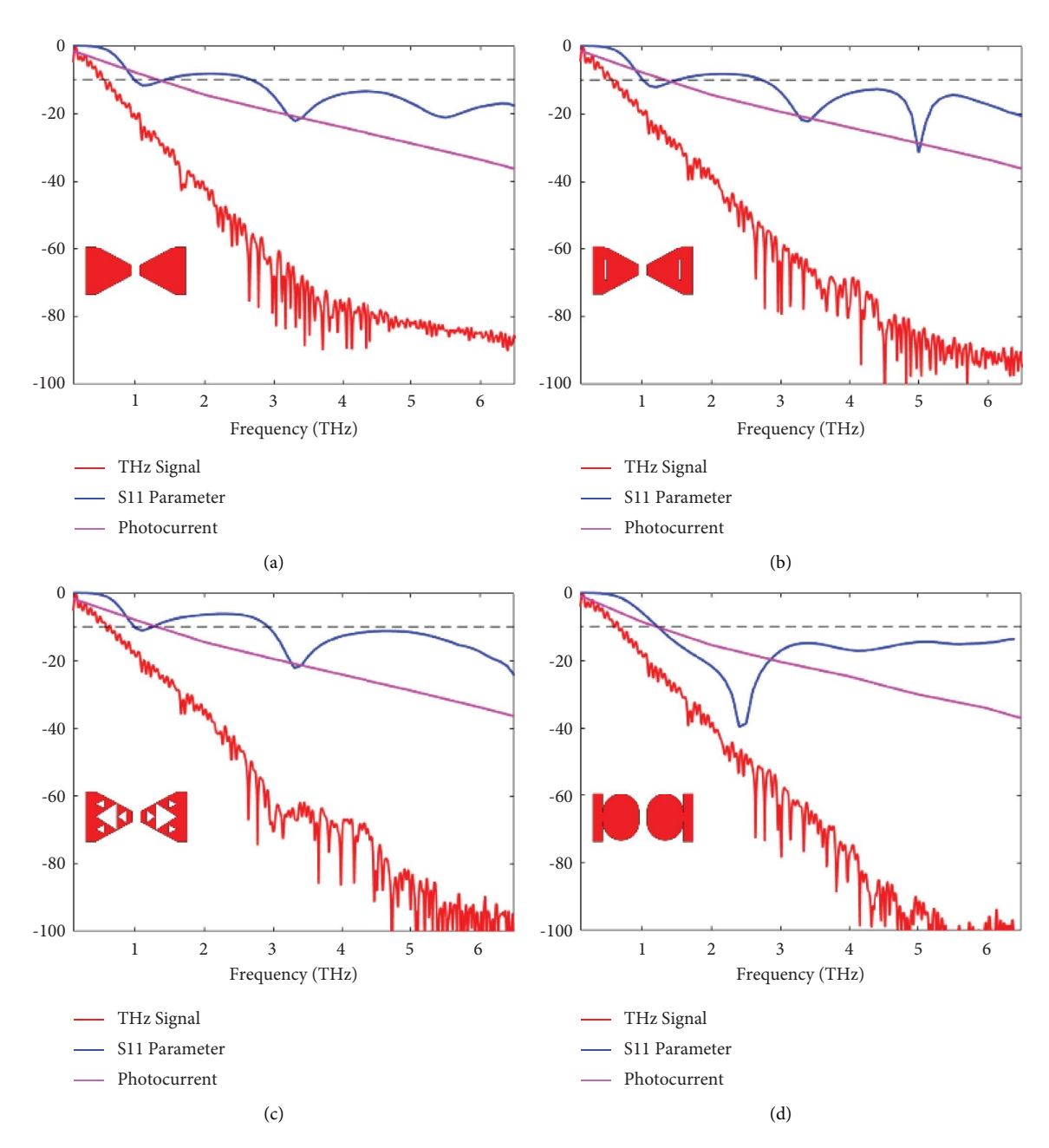


FIGURE 12: Analysis of overall bandwidth of measured THz signal based on the calculated  $S_{11}$  parameter and the calculated photoconductive current density for (a) bowtie, (b) slotted, (c) fractal, and (d) circular PCAs. Dashed line represents the  $-10 \, dB$  value. All generated THz signals in the figures are obtained through experimental measurement.

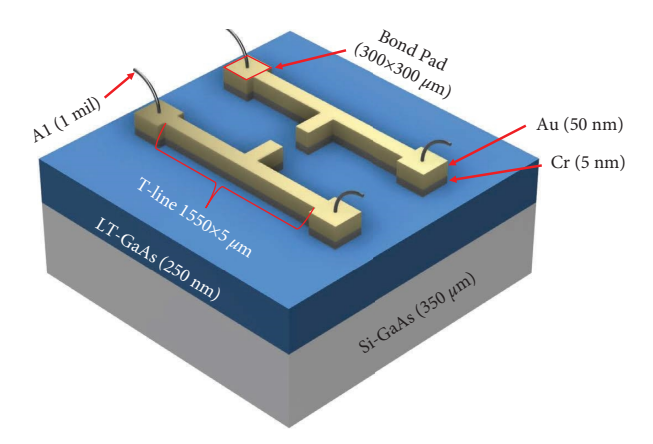


FIGURE 13: Fabricated 3D model of THz PCA emitter device stack (not to scale). The metallic electrodes represented in yellow color in this sketch were fabricated in four different shapes as demonstrated in Figure 7.

#### 4. Conclusions

In this work, we investigated four PCAs on LT-GaAs substrate with different metallic electrode geometries of well-known broadband antennas in the microwave band. The antennas were modeled using COMSOL multiphysics. EBL was utilized to fabricate the PCAs due to its maskless process, however, if devices were to be fabricated in bulk, photolithography could be more efficient. The challenges of overexposure and over etching were resolved upon applying the PEC modulation software. The overexposed areas were all successfully patterned with the increased sharpness in the small corners of the electrodes. The results presented here were not taken in a nitrogen purged environment. It should be noted that measurements carried out on different days, even with the same alignment, can slightly differ due to the humidity in the air.

It should be noted that the photocurrent pulse mainly depends on the properties of the LT-GaAs semiconductor, i.e., the carrier mobility, density, and lifetime, the bias voltage, the gap size, and the power of the laser beam. On the other hand, the S<sub>11</sub> parameter depends on the geometry of the electrodes and the dielectric properties of the semi-insulating GaAs substrate in the THz frequency band. As discussed previously, the spectra of the photocurrent and S<sub>11</sub> parameters are considered the main factors that affect the overall bandwidth of the radiated THz signal of the PCA.

Reference LT-GaAs PCA emitters obtained from Tera-View Ltd along with pinholes of diameters 1 mm and 0.5 mm were used to calibrate the TDS system ,and verify the THz beam alignment before collecting THz signal data of the PCAs presented in this work.

To assess the quality of the generated THz signals, pinholes were used. A rule of thumb used by PCA commercial manufacturers to evaluate the quality of the PCA is to use pinholes and verify that the signal amplitude is reduced by no more than 50%. This rule was proven in the commercial PCAs, however, the pinholes cut ~60% of the signal amplitude in the case of the investigated four PCAs. The reason is that the growth properties of the LT-GaAs wafer used in the commercial PCAs has higher quality in mobility and carrier lifetime. The growth and annealing

processes are protected under the IP of TeraView that were not shared with the authors.

Special attention must be paid to the polarization of not only the emitter device, but also the detector, and incoming laser. An x-cut quartz crystal half-wave plate was used as a linear polarization rotator in order to isolate the horizontal and vertical components of the emitted THz pulse. This halfwave plate has a thickness of 1 mm, which corresponds to an operating frequency of ~3 THz.

The obtained results demonstrate that the S-parameter (S<sub>11</sub>) of the bowtie, slotted, and fractal electrodes show multiple frequency bands while the circular shows a single broadband, however, the overall bandwidths of generated THz pulse of the four PCAs are similar. Furthermore, the obtained experimental results of the bandwidth and the peak-peak-amplitudes of all four PCAs agree with the modeling results presented in [17].

#### **Appendix**

#### A. Device Excitation and Materials

A femtosecond laser with an x-polarized wave, 780 nm wavelength, ~94 ps pulse width, and ~85 mw average power was used to excite the PCAs. This femtosecond laser illuminates the antenna gap between the two metallic electrodes of size  $4 \, \mu \text{m} \times 5 \, \mu \text{m}$  as shown in Figure 7. The materials used in the fabrication were an LT-GaAs layer of 250 nm thickness grown on top of the semi-insulating GaAs wafer of thickness 350  $\mu \text{m}$ , in addition to adhering layer of chromium of thickness 5 nm between the gold electrodes of thickness 50 nm and the LT-GaAs layer. To connect the bias voltage to the electrodes, an aluminum (Al) wire bond of diameter 1 mil is used as shown in Figure 13. "The design of the device was accomplished using a COMSOL Multiphysics model based on several efforts reported in [1, 10, 11, 13, 17, 25]."

## **B. Some Aspects of the Computation Model**

The first step is running the frequency-domain RF module to solve Maxwell's equations. In this module, we used the scattering boundary conditions at certain boundaries and the perfect electric and magnetic conductors at the lines of symmetries. For example, in modeling the incident electric field at the top face of the computational domain, we used the scattering boundary condition. In addition, at the bottom of the domain, we also used the scattering boundary conditions where the semi-insulating layer was modeled as half space. The perfect electric conductor (PEC) and the perfect magnetic conductor (PMC) are used at the lines of symmetries (i.e., the *y*- and *x*-directions, respectively). Using PEC and PMC boundary conditioned helped to manage the prohibitive requirement of the computational time and memory in 3D multiscale configuration even when using supercomputers. The other two modules are the semiconductor module to solve the diffuse/drift equations and the RF transient to solve the radiation equation. To avoid repeating the details of the three modules, we refer the readers to the cited references [11, 13, 25].

# **Data Availability**

Data are available upon request; Zach Uttley (1st author) should be contacted at zputtley@uark.edu.

# **Conflicts of Interest**

The authors declare that they have no conflicts of interest.

# Acknowledgments

This research was funded from the NSF award # 1948255. The authors also acknowledge TeraView Ltd in UK for providing the TeraAlign TDS system used in this work. The authors are thankful to Dr. Morgan Ware and Ms. Nikita Gurjar for their help on the x-cut half-wave plate crystals used in polarization measurements. The authors would also like to acknowledge Dr. Baolai Liang from the Integrated Nanomaterial Lab (INML) at UCLA for growing the LT-GaAs wafers. The authors are grateful to Prof. Martin Mittendorff and his postdoctoral fellow Dr. Han for measuring the characteristics of the LT-GaAs wafers used in this work.

### References

- [1] N. M. Burford and M. O. El-Shenawee, "Review of terahertz photoconductive antenna technology," *Optical Engineering*, vol. 56, no. 1, Article ID 010901, 2017.
- [2] M. El-Shenawee, N. Vohra, T. Bowman, and K. Bailey, "Cancer detection in excised breast tumors using terahertz imaging and spectroscopy," *Biomedical Spectroscopy and Imaging*, vol. 8, no. 1-2, pp. 1-9, 2019.
- [3] H. Tataria, M. Shafi, A. F. Molisch, M. Dohler, H. Sjoland, and F. Tufvesson, "6G wireless systems: vision, requirements, challenges, insights, and opportunities," *Proceedings of the IEEE*, vol. 109, no. 7, pp. 1166–1199, 2021.
- [4] E. Castro-Camus and M. Alfaro, "Photoconductive devices for terahertz pulsed spectroscopy: a review [Invited]," *Photonics Research*, vol. 4, no. 3, pp. A36–A42, 2016.
- [5] S. Gupta, M. Y. Frankel, J. A. Valdmanis et al., "Subpicosecond carrier lifetime in GaAs grown by molecular beam

- epitaxy at low temperatures," *Applied Physics Letters*, vol. 59, no. 25, pp. 3276–3278, 1991.
- [6] P. Maraghechi and A. Y. Elezzabi, "Fractal structures for THz radiation emitters," *IEEE Journal of Selected Topics in Quantum Electronics*, vol. 19, no. 1, Article ID 8400310, 2013.
- [7] J. Zhang, M. Tuo, M. Liang, X. Wang, and H. Xin, "Contribution assessment of antenna structure and in-gap photocurrent in terahertz radiation of photoconductive antenna," *Journal of Applied Physics*, vol. 124, no. 5, Article ID 053107, 2018.
- [8] C. W. Berry, M. R. Hashemi, and M. Jarrahi, "Generation of high-power pulsed terahertz radiation using a plasmonic photoconductive emitter array with logarithmic spiral antennas," *Applied Physics Letters*, vol. 104, no. 8, Article ID 081122, 2014.
- [9] M. F. Abdullah, A. K. Mukherjee, R. Kumar, and S. Preu, "Vivaldi end-fire antenna for THz photomixers," *Journal of Infrared, Millimeter and Terahertz Waves*, vol. 41, no. 6, pp. 728–739, 2020.
- [10] N. M. Burford, M. J. Evans, and M. O. El-Shenawee, "Plasmonic nanodisk thin-film terahertz photoconductive antenna," *IEEE Transactions on Terahertz Science and Technology*, vol. 8, no. 2, pp. 237–247, 2018.
- [11] J. S. Batista, H. O. H. Churchill, and M. El-Shenawee, "Black phosphorus photoconductive terahertz antenna: 3D modeling and experimental reference comparison," *Journal of the Optical Society of America B*, vol. 38, no. 4, pp. 1367–1379, 2021.
- [12] Y. Hirota, R. Hattori, M. Tani, and M. Hangyo, "Polarization modulation of terahertz electromagnetic radiation by four-contact photoconductive antenna," *Optics Express*, vol. 14, no. 10, pp. 4486–4493, 2006.
- [13] J. Santos Batista, "Computational modeling of black phosphorus terahertz photoconductive antennas using COMSOL Multiphysics with experimental comparison against a commercial LT-aAs emitter" M.S. ThesisUniversity of Arkansas, ProQuest, Fayetteville, AR, USA, 2021.
- [14] J. T. M. Stevenson and A. M. Gundlach, "The application of photolithography to the fabrication of microcircuits," *Journal* of *Physics E: Scientific Instruments*, vol. 19, 1986.
- [15] Y. Chen, "Nanofabrication by electron beam lithography and its applications: a review," *Microelectronic Engineering*, vol. 135, pp. 57–72, 2015.
- [16] Z. Uttley and M. El-Shenawee, "Fabrication and measurement of LT-GaAs photoconductive THz broadband antennas," in Proceedings of the 2022 IEEE International Symposium on Antennas and Propagation and USNC-URSI Radio Science Meeting (AP-S/URSI), Denver, CO, USA, July 2022.
- [17] J. Santos Batista and M. El-Shenawee, "Investigation of photoconductive antenna electrodes on terahertz signal generation," in *Proceedings of the 2021 IEEE International Symposium on Antennas and Propagation and USNC-URSI Radio Science Meeting (APS/URSI)*, Singapore, December 2021
- [18] P. K. Benicewicz, J. P. Roberts, and A. J. Taylor, "Scaling of terahertz radiation from large-aperture biased photoconductors," *Journal of the Optical Society of America B*, vol. 11, no. 12, pp. 2533–2546, 1994.
- [19] N. Burford, "Design, fabrication and measurement of a plasmonic enhanced terahertz photoconductive antenna," Ph.D. dissertation, University of Arkansas, Fayetteville, AR, USA, 2016.

- [20] J. T. Fourkas, "Nanoscale photolithography with visible light," Journal of Physical Chemistry Letters, vol. 1, no. 8, pp. 1221– 1227, 2010.
- [21] M. Horák, K. Bukvišová, V. Švarc, J. Jaskowiec, V. Krapek, and T. Sikola, "Comparative study of plasmonic antennas fabricated by electron beam and focused ion beam lithography," *Scientific Reports*, vol. 8, no. 1, 2018.
- [22] S. Freer, A. Gorodetsky, and M. Navarro-Cia, "Beam profiling of a commercial lens-assisted terahertz time domain spectrometer," *IEEE Transactions on Terahertz Science and Technology*, vol. 11, no. 1, pp. 90–100, 2021.
- [23] C. Zheng, Y. Zhang, and L. Wang, "Propagation of vectorial Gaussian beams behind a circular aperture," *Optics & Laser Technology*, vol. 39, no. 3, pp. 598–604, 2007.
- [24] A. Yariv and P. Yeh, Optical Waves in Crystals Propagation and Control of Laser Radiation, John Wiley & Sons, Hoboken, NJ, USA, 1948.
- [25] M. H. Doha, J. I. Santos Batista, A. F. Rawwagah et al., "Integration of multi-layer black phosphorus into photoconductive antennas for THz emission," *Journal of Applied Physics*, vol. 128, no. 6, Article ID 063104, 2020.